Supplement of Biogeosciences, 17, 1745–1763, 2020
https://doi.org/10.5194/bg-17-1745-2020-supplement

Biogeosciences Open Access EGU

Supplement of

Impact of ambient conditions on the Si isotope fractionation in marine pore fluids during early diagenesis

Sonja Geilert et al.

Correspondence to: Sonja Geilert (sgeilert@geomar.de)

1. Supplementary figures to main text

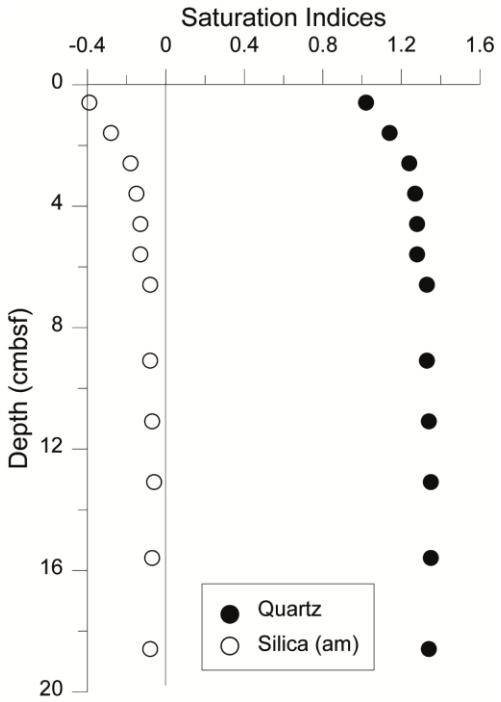

Fig. S1: Saturation indices calculated for amorphous silica (silica (am)) and quartz for the hydrothermal site using the program (PHREEQC).

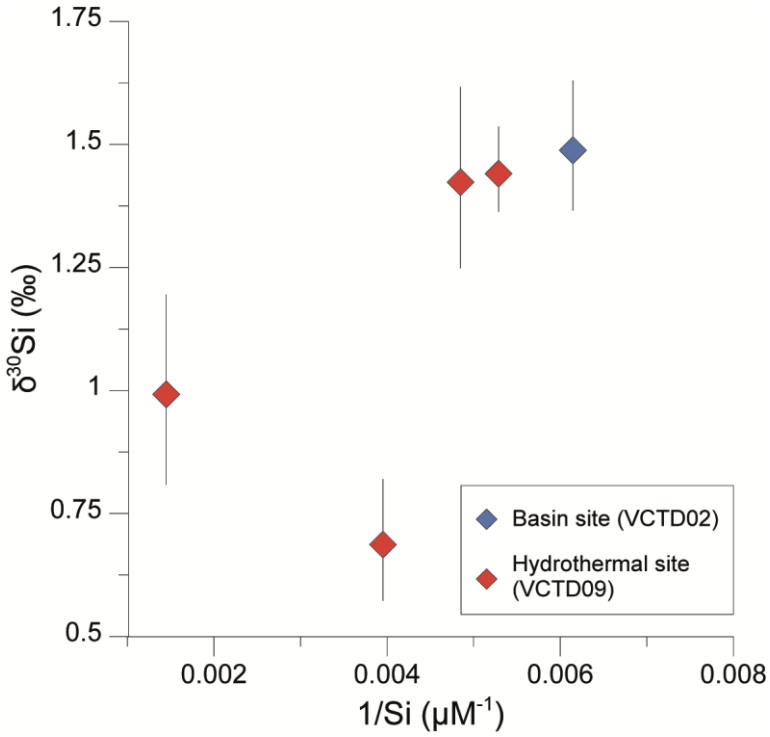

Fig. S2: Hydrothermal plume $\delta^{30}Si$ versus the Si concentration. For comparison the $\delta^{30}Si$ of the basin site water column is shown. No correlation with the Si concentration can be observed.

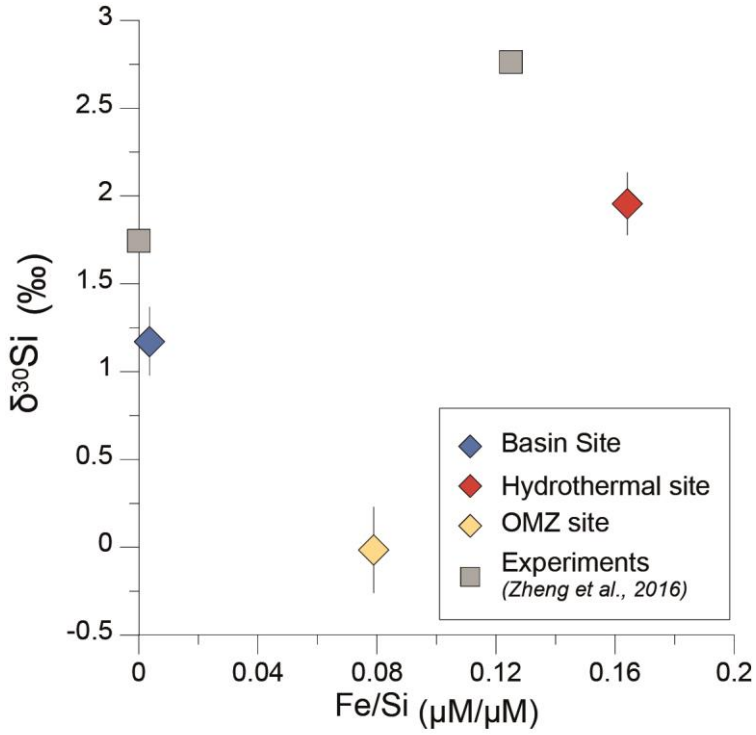

Fig. S3: The average $\delta^{30}Si$ values are displayed versus the Fe/Si ratio for the Guaymas Basin sites. Experimental results by Zheng et al. (2016) indicate that $\delta^{30}Si$ values should increase with the Fe/Si ratio in the solids and pore fluids. A similar trend exists for the basin sites and hydrothermal site indicating a possible Fe-induced fractionation. Data from the OMZ site, in contrast, deviate from this apparent trend (however, only based on two data points) and show lower $\delta^{30}Si_{pf}$ values as what would be expected regarding the Fe/Si ratio. This could be related to the likely one step fractionation during Fe-Si co-precipitation at the hydrothermal site and the existence of multiple Fe redox cycles inducing Si dissolution and re-precipitation and with that multiple fractionation steps at the OMZ site (see main text, section 4.3.3). Furthermore, any Fe-induced Si isotope fractionation is likely superimposed by the dissolution of terrigenous clays as shown by the reactive transport model. Natural Fe-induced Si isotope fractionation needs further investigation in future studies in order to be able to identify magnitudes of fractionation if other fractionating processes take place simultaneously.

2. Supplementary tables to main text

Table S1: Pore fluid and sediment geochemistry data

Station/MUC#/ Station name	Latitude (N) / Longitude (W)	Pore fluid						Sediment		
		Depth	Cl	Mg	Na	K	NH_4	TC	TOC	$CaCO_3$
		(cmbsf)	(mM)	(mM)	(mM)	(mM)	(µM)	%	%	%
SO241-33/11/	27° 33.301'	0	*557.8*	*53.9*	10.0	473	*0.98*			
Basin site	111° 32.883'	0.5	*553.7*	*53.4*	10.3	470	*7.49*	4.3	3.9	3.6
		1.5	*555.9*	*53.2*	10.4	471	*13.58*	4.3	3.9	3.8
		2.5	*564.6*	*53.5*	10.6	472	*11.06*	4.3	3.7	5.1
		3.5	*562.6*	*53.6*	10.7	475	*12.06*	-	-	-
		4.5	*567.2*	*53.1*	10.6	472	*11.26*	4.2	3.6	4.5
		6	*569.9*	*53.1*	10.6	472	*13.05*	3.3	3.0	2.8
		8	*570.9*	*52.7*	10.7	470	*13.51*	-	-	-
		10	*569.9*	*52.4*	10.7	469	*12.92*	-	-	-

		12.5	*568.9*	*52.2*	10.9	468	*13.18*	3.8	3.1	5.7
		15.5	*573.5*	*51.9*	10.8	469	*17.02*	3.6	3.1	4.2
		18.5	*569.1*	*51.5*	10.7	466	*19.47*	-	-	-
		22	*573.2*	*51.4*	10.7	468	*18.15*	4.2	3.2	8.5
SO241-22/04/	27° 28.165'	0	*573.5*	*54.1*	10.0	478	*0.0*	-	-	-
Basin site	111° 28.347'	0.5	*554.1*	*53.6*	10.3	475	*4.9*	5.9	5.1	6.1
		1.5	*557.1*	*53.3*	10.3	474	*8.4*	-	-	-
		2.5	*559.7*	*53.2*	10.4	473	*11*	7.1	5.3	15
		3.5	*554.7*	*53.2*	10.3	473	*11*	-	-	-
		4.5	*556.4*	*53.2*	10.3	474	*25*	-	-	-
		5.5	*558.4*	*52.9*	10.3	471	*28*	5.9	5.3	5.1
		7	*556.9*	*53.3*	10.4	475	*35*	-	-	-
		9	*558.7*	*53.1*	10.4	473	*49*	5.8	5.2	4.6
		11	*561.3*	*53.1*	10.3	473	*36*	-	-	-
		13	*558.1*	*53.2*	10.3	473	*43*	-	-	-
		15.5	*558.7*	*53.3*	10.4	475	*44*	-	-	-
		18.5	*558.3*	*53.0*	10.4	473	*33*	6.1	5.7	3.9
		22	*556.6*	*53.0*	10.4	473	*28*	-	-	-
		26	*559.8*	*53.2*	10.4	475	*21*	3.9	3.5	3.8
SO241-23/05/	27° 30.282'	0	*560.4*	*55.3*	10.3	489	*0.3*	-	-	-
Basin site	111° 40.770'	0.5	*556.3*	*53.5*	10.1	474	*0.2*	5.0	3.4	13
		1.5	*552.2*	*53.7*	10.2	477	*5.6*	-	-	-
		2.5	*565.1*	*53.2*	10.3	474	*16*	-	-	-
		3.5	*557.3*	*53.5*	10.3	475	*19*	5.2	3.8	12
		4.5	*562.2*	*53.5*	10.4	476	-	-	-	-
		5.5	*557.4*	*53.3*	10.3	474	*28*	5.6	4.0	14
		7	*561.4*	*53.3*	10.3	473	*26*	-	-	-
		9	*563.2*	*53.7*	10.4	479	*29*	5.6	4.2	12
		11	*566.2*	*53.4*	10.4	476	*25*	-	-	-
		13	*563.3*	*53.3*	10.4	475	*27*	-	-	-
		15.5	*563.4*	*53.3*	10.4	474	-	7.1	3.4	31
		18.5	*561.5*	*53.4*	10.4	476	-	-	-	-
		22	*565.7*	*53.1*	10.4	473	*47*	7.8	3.3	38
SO241-15/02/	27°26.925'	0	*566.1*	*54.3*	10.1	479	*0.0*	-	-	-
Basin site	111°29.926'	0.5	*560.7*	*53.5*	10.2	474	*1.0*	3.5	2.9	4.5
		1.5	*559.8*	*53.6*	10.2	474	*0.0*	3.7	3.1	5.2
		2.5	*565.0*	*53.4*	10.3	473	*0.0*	4.1	3.4	5.1
		3.5	*561.9*	*53.6*	10.3	475	*0.0*	4.1	3.4	5.6
		4.5	*565.2*	*53.2*	10.3	473	*0.4*	3.9	3.2	5.4
		5.5	*564.5*	*53.3*	10.4	474	*1.3*	4.1	3.3	5.9
		7	*557.4*	*53.0*	10.4	472	*3.6*	4.0	3.3	6.1
		9	*557.6*	*53.1*	10.5	472	*6.7*	3.8	3.1	6.0
		11	*553.6*	*53.3*	10.4	472	*8.0*	3.5	2.8	5.8
		13	*560.1*	*53.3*	10.4	472	*10*	3.4	2.7	5.7
		15.5	*559.2*	*53.4*	10.3	473	*15*	2.5	2.0	4.6
		18.5	*559.5*	*53.4*	10.3	473	*22*	2.3	1.8	4.0
		22	*556.6*	*53.3*	10.4	474	*31*	3.7	3.1	5.5
		26	*556.8*	*53.2*	10.5	473	*42*	3.5	2.8	5.8
		30	*555.3*	*53.3*	10.9	477	*53*	3.0	2.6	3.9
SO241-66/16/	27° 24.577'	0	*546.4*	*54.4*	10.2	480	*0.0*	-	-	-
Hydrothermal	111° 23.265'	0.5	*556.7*	*53.5*	10.3	474	*5.0*	2.4	2.2	1.8
site		1.5	*550.6*	*53.7*	10.4	477	*10*	2.5	2.3	2.0

		2.5	*548.6*	*53.5*	10.4	474	*16*	2.4	2.0	2.9
		3.5	*548.4*	*53.5*	10.4	476	*17*	2.2	2.0	1.6
		4.5	*557.1*	*53.6*	10.4	477	*20*	2.2	1.8	3.1
		5.5	*547.2*	*53.5*	10.4	477	*20*	2.0	1.8	1.7
		6.5	*547.9*	*53.4*	10.4	475	*21*	1.9	1.7	1.6
		9	*546.8*	*53.8*	10.4	478	*22*	1.6	1.4	1.6
		11	*554.6*	*53.5*	10.3	474	*22*	1.1	1.0	0.4
		13	*548.2*	*53.5*	10.2	474	*22*	1.9	1.8	0.9
		15.5	*549.2*	*53.6*	10.2	475	*20*	2.2	2.1	1.3
		18.5	*554.7*	*53.7*	10.2	476	*20*	0.3	0.3	0.3
SO241-29/09/	27° 42.410	0	557.9	54.1	474	10.1	4.7	-	-	-
OMZ site	111° 13.656	0.5	553.1	53.7	471	10.2	24	3.5	2.8	5.7
		1.5	552.6	53.7	471	10.2	50	3.9	3.1	6.8
		2.5	558.8	53.4	468	10.1	68	4.1	3.3	7.0
		3.5	556.5	53.8	472	10.2	58	4.1	3.2	7.1
		4.5	553.0	53.5	469	10.2	93	4.3	3.4	7.7
		5.5	551.2	53.8	475	10.3	73	4.6	3.5	8.9
		6.5	553.3	53.3	467	10.2	92	4.4	3.5	7.3
		7.5	552.6	53.5	471	10.2	139	4.2	3.4	6.9
		9	554.0	53.6	471	10.3	183	4.1	3.3	6.2
		11	553.7	53.7	472	10.3	218	4.0	3.4	5.0
		13	555.7	53.3	469	10.2	281	4.0	3.5	4.3
		15	557.7	53.4	471	10.3	320	4.0	3.4	5.1
		18.5	556.2	53.5	472	10.3	402	3.6	3.3	2.5
		20.5	551.8	54.2	477	10.5	480	3.8	3.5	2.3
		23.5	546.9	53.0	466	10.2	582	3.6	3.1	4.6
		26.5	551.3	52.9	465	10.2	606	4.0	3.4	5.3
		29	555.5	53.3	469	10.2	660	3.9	3.5	3.4
		30	556.2	53.4	469	10.2	702	3.5	3.2	2.4
		38	562.7	53.2	469	10.2	767	3.4	3.3	0.7

Italic numbers published in Geilert et al., 2018

Table S2: Main mineral phases identified by XRD analysis in wt% for the basin sites and the hydrothermal site.

Station/MUC#/ Station name	Depth	Quartz	Plagioclase	K-feldspar	Calcite	Mg-rich Calcite	Aragonite	Dolomite	Ankerite
Error (rel%)	(cmbsf)	±1	±2-5	±2-5	±1	±2-3	±2-3	±1	±2-3
SO241-33/11/	0.5	8.9	8.5	10.0	0.0	0.0	0.0	0.0	0.0
Basin site	2.5	6.2	5.4	7.6	0.0	0.0	0.0	0.0	0.0
	12.5	8.3	9.9	0.0	0.0	0.0	0.0	0.0	0.0
	22.0	7.7	9.2	5.1	0.0	0.0	0.0	0.0	0.2
SO241-22/04/	0.5	10.7	14.5	1.1	0.0	0.0	0.0	0.0	0.7
Basin site	5.5	14.0	16.6	4.9	0.0	0.0	0.0	0.0	0.7
	9.0	8.9	7.6	10.3	0.0	0.3	0.0	0.0	0.4
	18.5	9.5	10.4	13.6	0.0	0.0	0.0	0.0	0.6
	26.0	9.0	10.0	9.8	0.0	0.0	0.0	0.0	0.3
SO241-23/05/	0.5	7.2	8.4	0.0	0.0	0.0	0.0	0.0	0.4
Basin site	3.5	6.9	5.7	17.7	0.0	0.0	0.0	0.0	0.5
	9.0	8.5	6.6	4.6	0.0	0.0	0.0	0.3	0.0
	22.0	9.0	10.1	4.3	0.2	0.4	0.0	0.3	0.4
SO241-15/02/	0.5	3.0	6.2	5.7	0.0	0.0	0.0	0.2	0.3
Basin site	5.5	9.1	9.0	1.7	0.0	0.7	0.0	0.0	0.4
	15.5	15.5	8.2	0.0	0.0	0.4	0.0	0.1	1.0
	30.0	8.2	9.6	2.7	0.0	0.0	0.0	0.0	0.5
SO241-66/16/	0.5	2.0	19.8	5.8	0.0	0.0	0.0	0.0	0.0
Hydrothermal	2.5	9.1	9.8	19.5	0.0	0.0	0.0	0.2	0.3

site	5.5	7.8	12.3	10.7	0.4	0.4	0.0	0.4	0.4
	13.0	0.8	4.8	9.5	0.0	0.0	2.6	0.4	0.4
	18.5	1.9	12.5	22.9	0.5	0.5	0.0	0.7	0.2

Table S2 continued

Station/MUC#/ Station name	Depth	Smectites	Montmorillo -nites	Cristoballite	Trydimite	SiO2 nearly amorphous	Mixed Layer Clays	Illites	Muscovite	Biotite	Glauconite	Kaolinite	Chlorite
Error (rel%)	(cm bsf)	±5-10	±5-10	±2	±2	±5-10	±5-10	±5-10	±5-10	±5-10	±5-10	±2-5	±2-5
SO241-33/11/	0.5	0.0	5.0	0.0	0.0	23.9	20.3	5.9	1.7	0.0	0.0	1.9	1.0
Basin site	2.5	0.0	20.8	0.0	2.4	20.4	3.5	7.1	2.2	1.7	0.0	4.5	1.0
	12.5	1.4	6.6	0.0	0.0	22.6	25.0	7.0	0.0	0.0	0.0	1.9	0.8
	22.0	1.5	7.7	0.0	0.0	28.1	14.0	4.8	0.0	0.0	0.0	3.4	0.7
SO241-22/04/	0.5	3.4	7.2	0.0	0.0	8.0	2.3	26.0	0.0	0.0	0.0	4.9	1.0
Basin site	5.5	1.9	1.8	0.0	0.0	4.5	13.2	17.1	0.0	0.0	0.0	5.3	1.0
	9.0	0.5	7.4	0.0	0.0	5.0	7.3	36.6	0.0	1.5	0.0	4.5	1.0
	18.5	0.0	6.6	0.7	0.0	4.4	0.0	20.9	0.0	6.0	0.0	4.1	3.0
	26.0	0.0	7.1	0.0	0.0	4.7	7.6	10.9	2.9	2.0	0.0	6.0	0.8
SO241-23/05/	0.5	1.3	2.4	2.7	0.0	35.8	9.6	6.7	0.0	0.0	3.3	3.5	0.6
Basin site	3.5	6.3	5.2	0.0	0.0	41.0	5.5	8.7	0.0	0.0	4.3	6.4	0.5
	9.0	1.7	4.6	0.0	0.0	25.4	11.8	9.8	0.0	0.0	1.8	4.7	1.1
	22.0	1.1	4.0	0.0	0.0	23.0	15.4	5.6	0.0	0.0	0.0	5.9	0.7
SO241-15/02/	0.5	1.2	6.3	0.0	0.0	10.2	25.9	0.0	0.0	0.0	0.0	1.7	2.8

Basin site	5.5	2.9	7.5	0.0	0.0	28.6	8.6	12.6	0.0	0.0	0.0	3.6	1.8
	15.5	0.0	0.0	0.0	0.0	57.1	0.0	4.8	4.2	0.0	0.0	3.0	1.0
	30.0	3.5	6.9	0.0	0.0	21.7	5.9	9.3	0.0	0.0	3.6	4.1	1.3
SO241-66/16/	0.5	0.0	5.7	0.0	0.0	42.8	0.0	12.8	0.0	0.0	0.0	3.0	0.7
Hydrothermal site	2.5	2.6	8.0	1.6	1.6	25.3	5.0	14.3	0.0	0.0	1.4	3.9	0.6
	5.5	0.0	12.3	0.0	0.0	26.2	19.9	0.0	0.0	0.0	0.0	5.4	0.3
	13.0	0.0	1.9	0.0	0.0	42.2	4.0	5.1	0.0	0.0	0.0	3.0	2.5
	18.5	0.0	4.4	0.0	0.5	40.4	5.0	4.4	0.0	0.0	0.0	2.3	0.6

Table S2 continued

Station/MUC#/ Station name	Depth	Clino-Pyroxenes	Ortho-Pyroxenes	Pyrites	Fe-Oxides Fe-Hydroxides, Manganit	Barite
Error (rel%)	(cm bsf)	±2-5	±2-5	±2-5	±5-10	±2-5
SO241-33/11/	0.5	1.05	8.25	0.00	0.40	0.00
Basin site	2.5	1.45	2.82	2.44	0.00	0.00
	12.5	0.00	5.21	0.00	0.00	0.00
	22.0	4.71	0.00	3.67	1.33	0.00
SO241-22/04/	0.5	4.99	0.00	0.00	2.55	0.00
Basin site	5.5	3.98	0.00	0.15	2.56	0.00
	9.0	0.00	0.00	0.00	3.57	0.00
	18.5	5.70	0.87	6.50	1.49	0.00
	26.0	3.74	0.84	0.00	0.86	0.00

SO241-23/05/	0.5	0.00	0.00	0.19	9.49	0.18
Basin site	3.5	0.00	0.00	0.34	0.77	0.00
	9.0	2.03	0.00	0.00	4.17	0.00
	22.0	0.65	0.00	0.00	3.73	0.00
SO241-15/02/	0.5	0.00	13.78	4.33	3.09	0.00
Basin site	5.5	3.13	0.00	0.00	0.51	0.00
	15.5	1.10	0.00	1.77	0.29	0.36
	30.0	0.57	0.00	0.25	0.43	0.00
SO241-66/16/	0.5	0.00	0.00	0.48	1.74	1.21
Hydrothermal site	2.5	0.00	2.58	0.00	2.37	0.00
	5.5	0.00	0.00	0.00	1.03	0.19
	13.0	0.00	4.59	3.58	0.23	1.38
	18.5	1.07	1.82	0.53	0.00	1.79

3.1 Model set-up

The turnover of solids (S) and dissolved species (P) was simulated applying the following mass balance equations:

$$d_S \cdot (1-\Phi) \cdot \frac{\partial S}{\partial t} = \frac{\partial}{\partial x}\left(d_S \cdot (1-\Phi) \cdot \left(D_B \cdot \frac{\partial S}{\partial x} - w \cdot S \right)\right) + d_S \cdot (1-\Phi) \cdot R_S$$

$$\Phi \cdot \frac{\partial P}{\partial t} = \frac{\partial}{\partial x}\left(\Phi \cdot \left(D_S \cdot \frac{\partial P}{\partial x} - v \cdot P \right)\right) + \Phi \cdot R_D$$

with S: concentration of solid species in dry sediment (g g^{-1}), P: concentration of dissolved species in pore water (µmol cm^{-3}), t: time (yr), x: sediment depth (cm), d_S: density of dry solids (d_S = 2.5 g cm^{-3}), Φ: porosity, D_B: bioturbation coefficient (cm^2 yr^{-1}); w: burial velocity of solids (cm yr^{-1}); R_S: turnover rates of solid species (g g^{-1} yr^{-1}), R_D: turnover rates of dissolved species (mmol cm^{-3} yr^{-1}), D_S: molecular diffusion coefficient of dissolved species in sediment pore water (cm^2 yr^{-1}); v: burial velocity of pore water (cm yr^{-1}).

The model was set up for 5 solid species (SiO_2 in biogenic opal, SiO_2 in authigenic phases, K in sediments, $^{30}SiO_2$ in biogenic opal, $^{30}SiO_2$ in authigenic phases) and 3 species dissolved in porewater (silica, ^{30}Si-silica, K).

At the upper boundary of the model (x = 0), constant fluxes (rain rates RR_S) were applied for the solids:

$$d_S \cdot (1-\Phi) \cdot \left(-D_B \cdot \frac{\partial S}{\partial x} + w \cdot S \right)\Big|_{x=0} = RR_S$$

whereas constant concentrations corresponding to ambient bottom water values (P_{BW}) were used for the solutes:

$$P\big|_{x=0} = P_{BW}$$

A zero gradient condition was applied at the lower boundary (x = L) for both solids and solutes:

$$\frac{\partial S}{\partial x}\bigg|_{x=L} = 0 \qquad \frac{\partial P}{\partial x}\bigg|_{x=L} = 0$$

The model was solved using the solver for partial differential equations of MATHEMATICA applying the Method-of-Lines approach. The model was integrated over time until a steady state was attained. Parameter values, depth-dependent functions, kinetic rate laws, and rate terms applied in the model are listed in Tables S3- S6.

Our model is based on a previously developed isotope model to simulate the reactive transport of dissolved silica in surface sediments (Ehlert et al., 2016). In the previous model, two separate mass balance equations (see above) were set up to simulate the turnover of total dissolved $^{30}SiO_2$ and SiO_2. The isotopic composition of the pore fluid was calculated as ratio of these two compounds (MF_{30} = $^{30}Si/Si$). Considering the abundance of the three Si isotopes ^{28}Si, ^{29}Si and ^{30}Si, the mol fraction MF_{30} is related to the commonly used isotope ratio (R_{30} = $^{30}Si/^{28}Si$) as:

$$R_{30} = \frac{MF_{30} \cdot R_{St30} \cdot (R_{St29} \cdot (c_R - 1) - 1)}{c_R \cdot MF_{30} \cdot R_{St29} + R_{St30} \cdot (MF_{30} - 1)}$$

with R_{St30} = 0.0341465, R_{St29} = 0.0507446 and c_R = 0.51 (Ehlert et al., 2016).

The $\delta^{30}Si$ value of the pore fluid (in ‰) is calculated from the ratio as:

$$\delta^{30}Si = \left(\frac{R_{30}}{R_{St30} - 1}\right) \cdot 1000$$

Concentrations of biogenic opal, K/Al ratios in bulk sediment and the concentration and isotopic composition of dissolved silica determined in pore fluids were employed to constrain rates of opal and terrigenous phase dissolution and the precipitation rate of authigenic phases. The isotopic composition of dissolved silica in bottom water at the OMZ site ($\delta^{30}Si_{bw}$ = +0.81 ‰) is close to the isotopic composition of biogenic opal measured in OMZ sediments ($\delta^{30}Si_{bSiO2}$ = +0.77 ‰). Hence, opal dissolution did not induce the significant shift in the pore fluid composition. The shift to negative values observed in the pore fluids ($\delta^{30}Si_{pf}$) within the top cm of the sediment column is caused by the dissolution of terrigenous phases depleted in ^{30}Si. We applied a $\delta^{30}Si_{terr}$ value of -2 ‰ to simulate the release of depleted terrigenous Si like clays into the pore fluids and induce the negative shift observed in the data. Authigenic phases precipitating in marine sediments are depleted in ^{30}Si with respect to the pore fluids. We applied a fractionation factor of Δ_{Au} = -2 ‰ (Δ_{Au} = $\delta^{30}Si_{au}$ - $\delta^{30}Si_{pf}$) to simulate the impact of authigenic phase precipitation on pore fluid composition as previously observed in Peruvian OMZ sediments (Ehlert et al., 2016). With this approach, the positive shift of $\delta^{30}Si_{pf}$ values observed below 1 cm sediment depth in Peruvian OMZ sediments was reproduced in the model by a combination of opal dissolution and authigenic phase precipitation.

The kinetics of terrigenous phase dissolution is largely known (Wallmann et al., 2008). Since our data imply that most of the dissolution takes place within the top cm of the sediment, we apply a dissolution rate that decreases exponentially with sediment depth (Fig. S4). Authigenic mineral precipitation is probably linked to terrigenous phase dissolution because dissolved Al released from terrigenous phases supports the formation of authigenic Si-Al phases in marine sediments (Loucaides et al., 2010). Hence, the precipitation rate usually decreases with sediment depth (Loucaides et al., 2010). Since the reactivity of biogenic opal also decreases with sediment depth (Van Cappellen and Qiu, 1997b), we assumed that the

kinetic rate constants for authigenic phase precipitation and biogenic opal dissolution decrease exponentially with depth (Tab. S4) and applied a solubility control to simulate the rates (Fig. S4, Tab. S5).

K/Al ratios measured in the solid phase and pore water K data were used as additional model constraints. We did not separate the pore water from the sediment prior to the solid phase K analysis. Hence, the K concentrations measured in the dried sediment samples were corrected for the contribution of K dissolved in pore fluids applying the following equation:

$$K_C = K_M - \frac{f_W}{1 - f_W} K_{PW}$$

where K_C is the concentration of K in the solid phase (g/g) corrected for the pore water contribution, K_M is the concentration of K measured in dried samples (g/g), f_W is the initial water content of the wet samples prior to drying (g/g) and K_{PW} is the concentration of dissolved K in the pore water (g/g). The concentration of K in pore water was measured in units of mmol/dm^3. It was converted into appropriate units (g/g) by multiplying with the factor 10^{-6} MW_K where MW_K is the molecular weight of K.

The release of K during the dissolution of terrigenous phases and the uptake of K in authigenic phases was simulated applying corresponding K/Si ratios. Unfortunately, we did not determine the Si content of the OMZ sediments. Moreover, the total Si content in OMZ sediments reflects not only the terrigenous contribution but also the concentrations of biogenic opal and authigenic phases. The mean K/Al ratio measured in our OMZ sediments (0.33 g/g, after correction for pore water K) is close to the K/Al ratio in shale (0.34 g/g) and upper continental crust (0.35 g/g) (Taylor and McLennan, 1995; Wedepohl, 1971). Hence, we applied the mean K/Si ratio of shale and upper continental crust to simulate the K release from terrigenous phases (K/Si_{Terr} = 0.1 g/g = 0.07 mol/mol). Authigenic Si phases formed in marine sediments are typically enriched in K and we applied the K/Si of authigenic material in Amazon sediments (Michalopoulos and Aller, 2004) to define the uptake of K in authigenic phases (K/Si_{Au} = 0.19 mol/mol).

Moreover, we applied a constant Al concentration in the model corresponding to the mean Al concentration measured in the OMZ sediments (4.8 ± 0.5 wt%). We assumed a constant Al deposition rate at the sediment surface and that Al released from sediments during mineral dissolution was quantitatively re-precipitated in authigenic minerals. The solid phase K concentrations calculated in the model were normalized to the mean Al concentration measured in the sediment and compared to the measured K/Al ratios. With this approach, we assume that any down-core change in the Al concentration observed in the data is induced by processes that are not considered in the model such as temporal changes in the composition and mass accumulation rate of terrigenous phases deposited at the sediment surface.

A best fit model solution was obtained by fitting the model results to dissolved silica concentrations and $\delta^{30}Si$ values measured in the pore fluids and the biogenic opal and K/Al ratios measured in the solid phase corrected for pore water K. Down-core changes in kinetic rate constants (Fig. S4, Tab. S4), rain rates of biogenic opal and solid phase K at the sediment surface and the solubility of the authigenic phase were varied systematically to obtain the best fit to the observations. However, care should be taken regarding the model results, given that we used strongly simplifying assumptions (e.g. steady state, simple rate laws). Additionally, our assumptions of solid phase reactivity and $\delta^{30}Si$ values are preliminary and not supported by independent data.

Tab. S3. Parameter values applied in the model

Parameter	**Symbol**	**Value**
Density of dry solids	d_S	2.5 g cm^{-3}
Porosity at x = 0	Φ_0	0.97
Porosity at x = infinity	Φ_f	0.91
Attenuation coefficient for porosity decrease	px	0.15 cm^{-1}
Bioturbation coefficient at x = 0	$D_B(0)$	1 cm^2 yr^{-1}
Depth of bioturbated zone	x_B	1 cm
Burial velocity after compaction	w_f	0.18 cm yr^{-1}
Sediment temperature	T	6.7 °C
Salinity of porewater	Sal	35
Molecular diffusion coefficient for dissolved silica	D_M	188 cm^2 yr^{-1}
Molecular diffusion coefficient for dissolved K	D_M	388 cm^2 yr^{-1}
Solubility of biogenic opal	Sol_{opal}	0.8 mM
Solubility of authigenic phase	Sol_{au}	0.2 mM
Rain rate of biogenic opal	RR_{opal}	7.3 mg cm^{-2} yr^{-1}
Rain rate of K	RR_K	0.77 mg cm^{-2} yr^{-1}
Molar K/Si ratio in terrigenous phase	K/Si_{terr}	0.07
Molar K/Si ratio in authigenic phase	K/Si_{au}	0.19
$\delta^{30}Si$ of opal deposited at the seafloor	$\delta^{30}Si_{opal}$	+0.77 ‰
$\delta^{30}Si$ of terrigenous phase subject to dissolution	$\delta^{30}Si_{terr}$	-2.0 ‰
Isotopic fraction factor for authigenic phase formation	Δ_{au}	-2.0 ‰
Isotopic fraction factor for authigenic phase formation in term of mol fractions	β_{au}	0.998111
Molecular weight of SiO_2	MW_{SiO2}	60.08 g mol^{-1}
Atomic weight of K	MW_K	39.098 g mol^{-1}

Tab. S4. Depth-dependent functions applied in the model

Parameter	Symbol	Equation
Porosity	Φ	$\Phi = \Phi_f + (\Phi_0 - \Phi_f) \cdot \exp(-px \cdot x)$
Bioturbation coefficient	D_B	$D_B = D_B(0) \cdot \exp\left(-\frac{x^2}{2 \cdot {x_B}^2}\right)$
Burial velocity of solids	w	$w = w_f \cdot \frac{1-\Phi_f}{1-\Phi}$
Burial velocity of solutes	v	$v = w_f \cdot \frac{\Phi_f}{\Phi}$
Tortuosity	To	$To^2 = 1 - 2 \cdot ln(\Phi)$
Diffusion coefficient of solutes in porewater	D_S	$D_S = \frac{D_M}{To^2} + D_B$
Function to convert rates from g g^{-1} yr^{-1} to µmol cm^{-3} yr^{-1}	f_{sp}	$f_{sp} = d_S \cdot 10^6 \cdot \frac{1-\Phi}{\Phi \cdot MW}$
Kinetic constant for biogenic opal dissolution (in yr^{-1})	k_{opal}	$k_{opal} = 0.03 \cdot e^{-0.05 \cdot x}$
Kinetic constant for terrigenous phase dissolution (in µmol cm^{-3} yr^{-1})	k_{terr}	$k_{terr} = 58 \cdot e^{-1.3 \cdot x}$
Kinetic constant for authigenic mineral precipitation (in µmol cm^{-3} yr^{-1})	k_{au}	$k_{au} = 5 \cdot e^{-0.5 \cdot x}$
Mol fraction of Si	MF	$MF = \frac{^{30}Si}{Si}$

Table S5: Kinetic rate laws applied in the model

Reaction	Symbol	Equation
Biogenic opal dissolution in g g^{-1} yr^{-1}	R_{opal}	$R_{opal} = k_{opal} \cdot S_{opal} \cdot \left(1 - \frac{Si(OH)_4}{Sol_{opal}}\right)$
Dissolution of terrigenous phase in µmol cm^{-3} yr^{-1}	R_{terr}	$R_{terr} = k_{terr}$
Authigenic mineral precipitation in µmol cm^{-3} yr^{-1}	R_{au}	$R_{au} = k_{au} \cdot \left(\frac{Si(OH)_4}{Sol_{au}} - 1\right)$
Dissolution of $^{30}SiO_2$ in biogenic opal in g g^{-1} yr^{-1}	$R_{opal}{}^{30}$	$R_{opal}{}^{30} = MF_{opal} \cdot R_{opal}$
Dissolution of terrigenous $^{30}SiO_2$ in µmol cm^{-3} yr^{-1}	$R_{terr}{}^{30}$	$R_{terr}{}^{30} = MF_{terr} \cdot R_{terr}$
Precipitation of authigenic $^{30}SiO_2$ in µmol cm^{-3} yr^{-1}	$R_{au}{}^{30}$	$R_{au}{}^{30} = MF_{pf} \cdot \beta_{au} \cdot R_{au}$

Table S6: Rate terms applied in mass balance equations

Species	**Equation**
Biogenic opal (in g g^{-1} yr^{-1})	$- R_{opal}$
Authigenic phase (in g g^{-1} yr^{-1})	$+ R_{au}/f_{sp}$
K in sediment (in g g^{-1} yr^{-1})	$(-K/Si_{terr}\ R_{terr} + K/Si_{au}\ R_{au})/f_{sp}$
Dissolved silica (in µmol cm^{-3} yr^{-1})	$f_{sp}\ R_{opal} + R_{terr} - R_{au}$
Dissolved K (in µmol cm^{-3} yr^{-1})	$K/Si_{terr}\ R_{terr} - K/Si_{au}\ R_{au}$
^{30}Si in authigenic phase (in g g^{-1} yr^{-1})	$+ R_{au}{}^{30}/f_{sp}$
^{30}Si in dissolved silica (in µmol cm^{-3} yr^{-1})	$f_{sp}\ R_{opal}{}^{30} + R_{terr}{}^{30} - R_{au}{}^{30}$

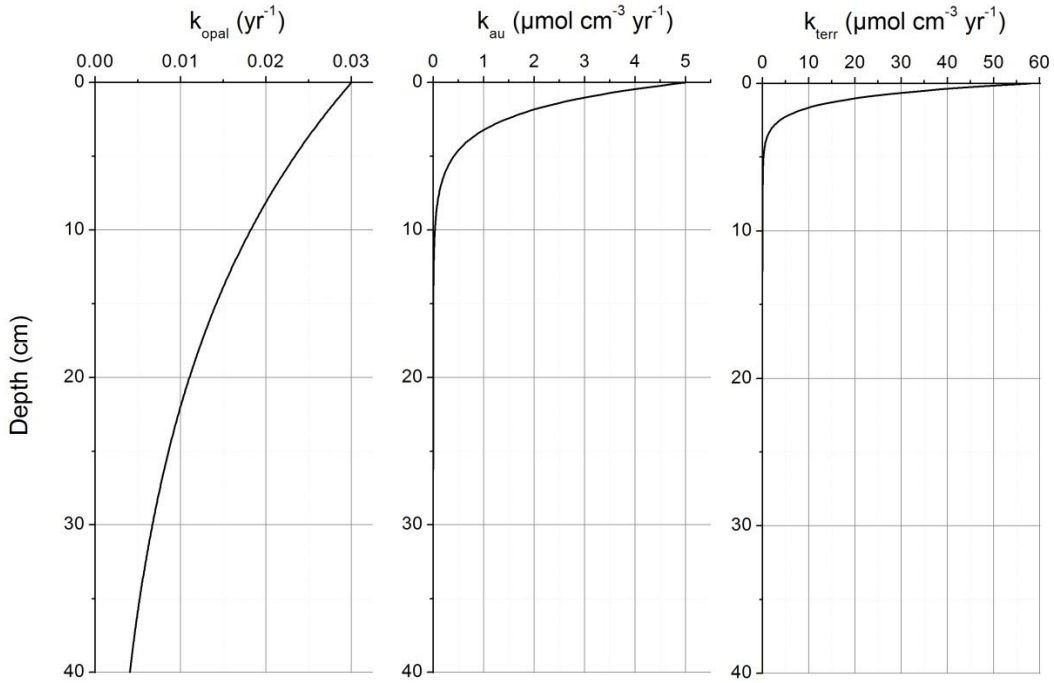

Fig. S4. Down-core profile of kinetic constants for biogenic opal dissolution (k_{opal}), authigenic phase precipitation (k_{au}) and terrigenous phase dissolution (k_{terr}) applied in the model runs.

3.2. Sensitivity tests

Key model parameter values were varied to study how they affect the model results and the fit to observations.

In the standard case presented in the main text, the molar K/Si ratio of authigenic phases that precipitate from the pore fluids (r_{KSiAu}) was defined as 0.19 as previously measured in authigenic phases forming in Amazon shelf sediments (Michalopoulos and Aller, 2004). We are not aware of any other study that quantified K/Si ratios of authigenic Si-Al-phases in continental margin sediments. Nevertheless, we varied this model parameter to investigate how the K/Al ratio of bulk sediments calculated in the model is affected by the r_{KSiAu} value. Two additional model runs with r_{KSiAu} = 0.14 and r_{KSiAu} = 0.24 were conducted. The resulting K/Al ratios deviate significantly from the results of the standard case and are not consistent with the K/Al ratios measured in bulk OMZ sediments (Fig. S5). The concentration of K dissolved in pore fluids is also affected by r_{KSiAu}. Due to the very high porosity of the OMZ surface sediments, the resulting changes are, however, so small (about 0.01 mM) that they cannot be resolved by pore fluid analysis. Other model outcomes are not affected because r_{KSiAu} does not control any of the reaction rates in the model. Considering the good fit obtained in the standard case applying r_{KSiAu} = 0.19, we conclude that the K/Si ratio of authigenic phases forming in our OMZ sediments is similar to that previously determined in Amazon shelf sediments (Michalopoulos and Aller, 2004).

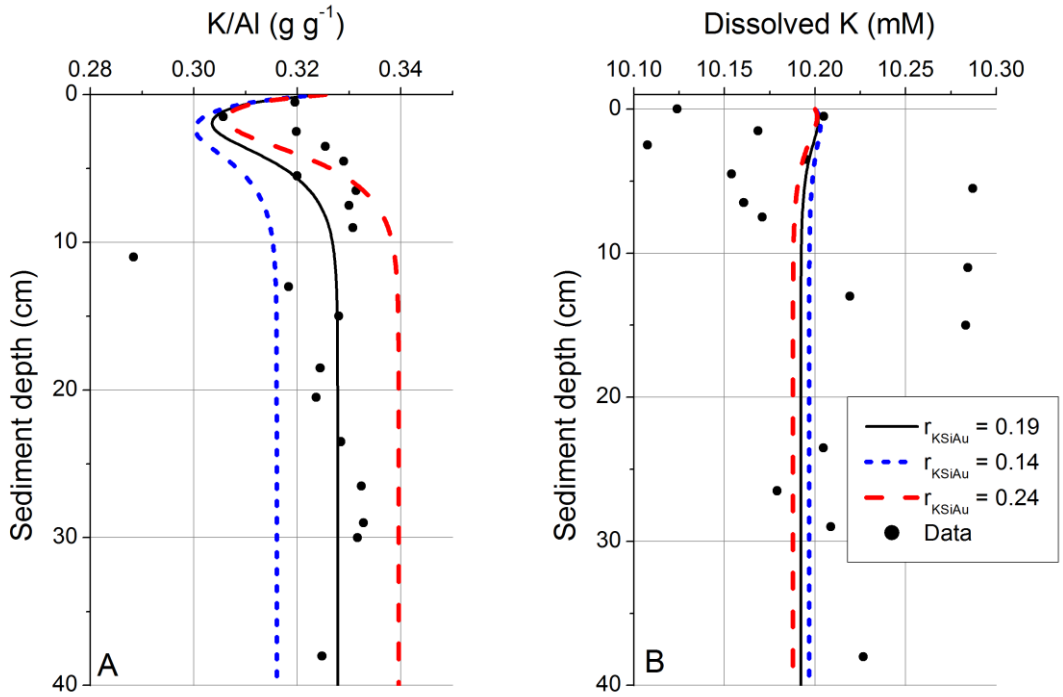

Fig. S5. Sensitivity of the model with respect to the K/Al ratio of authigenic phases. A. K/Al ratio in bulk sediment. B. Dissolved potassium in pore fluids. Data are compared to model results for the standard case (r_{KSiAu} = 0.19) and for two additional simulations with r_{KSiAu} = 0.14 and r_{KSiAu} = 0.24.

Further model runs were conducted to study how the isotopic composition of dissolved silica is controlled by the isotopic composition of dissolving solids and the isotopic fractionation that occurs during the precipitation of authigenic phases (Fig. S6). These simulations indicate that the terrigenous solids dissolving in the top cm of the sediment column need to be isotopically depleted with $\delta^{30}Si_{terr}$ ≈ -2 ‰ in order to reproduce the strong minimum observed in the pore fluid data. The surface minimum is not reproduced when less depleted values characteristic for clays as well as feldspars and other reactive silicates such as olivine are employed in the model ($\delta^{30}Si_{terr}$ = -1 ‰ to 0 ‰). We also varied the isotopic fractionation factor for authigenic mineral precipitation (Δ_{Au}). In the standard case, we used Δ_{Au} = - 2 ‰, a value that was previously derived for the Peruvian OMZ (Ehlert et al., 2016). We chose this value because the Peruvian study is the only one that determined Δ_{Au} for marine sediments. When less fractionation is assumed, the pore fluid values are shifted to lower values because more of the light isotope remains in solution. The surface minimum in the pore fluid data can be reproduced by dissolving solids that are somewhat less depleted ($\delta^{30}Si_{terr}$ ≈ -1.7 ‰) than in the standard case when a lower fractionation is employed (Δ_{Au} = - 1 ‰). However, also this less depleted value is characteristic for clay mineral dissolution (Frings et al., 2016). Hence, we conclude that isotopically depleted clays rather than primary silicates (e.g. feldspars with $\delta^{30}Si_{terr}$ close to 0 ‰) dissolve in the surface layer.

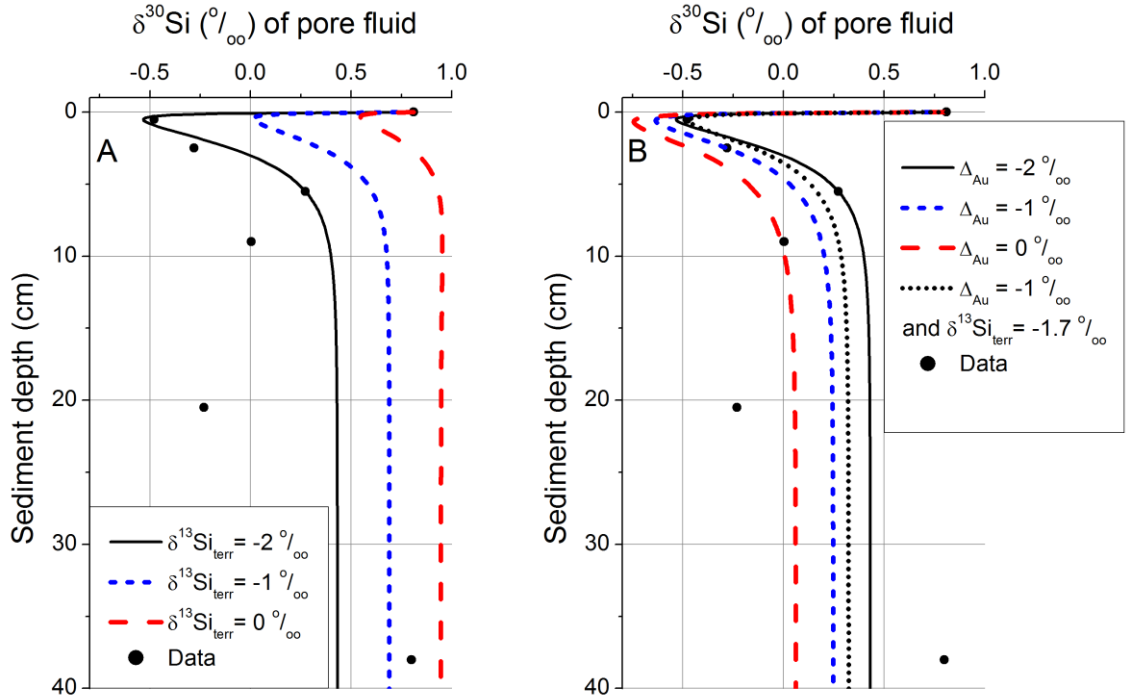

Fig. S6. $\delta^{30}Si$ of dissolved silica in pore fluids. A. Sensitivity of the model with respect to the isotopic composition of dissolving silicate phases (standard case: $\delta^{30}Si_{terr}$ = -2 ‰). B. Sensitivity of the model with respect to isotopic fractionation during the precipitation of silicate phases (standard case: Δ_{Au} = - 2 ‰).

In the standard case, we assumed that biogenic opal has a solubility of 800 µM because dissolved silica measured in the pore fluids attained a plateau value of about 800 µM at the base of the analyzed sediment core. An empirical equation for the temperature-dependent solubility of biogenic opal yields, however, a value of 957 µM for the ambient temperature of 6.7 °C in our OMZ sediments (Van Cappellen and Qiu, 1997a). Hence, we conducted an additional simulation applying the theoretical solubility value of 957 µM (Fig. S7). Due to the increase in solubility, the dissolved silica concentrations at depth rise to a plateau that clearly exceeds the measured values. The change in solubility induced a significant rise in the rate of authigenic phase precipitation because the oversaturation was enhanced by the increase in dissolved silica. The δ^{30}Si of dissolved silica and K/Al ratio in bulk sediments also increased due to the rise in the precipitation rate. In a final simulation, we increased the kinetic constant for precipitation to remove dissolved silica from the pore fluids and obtain concentrations that are consistent with the measured data.

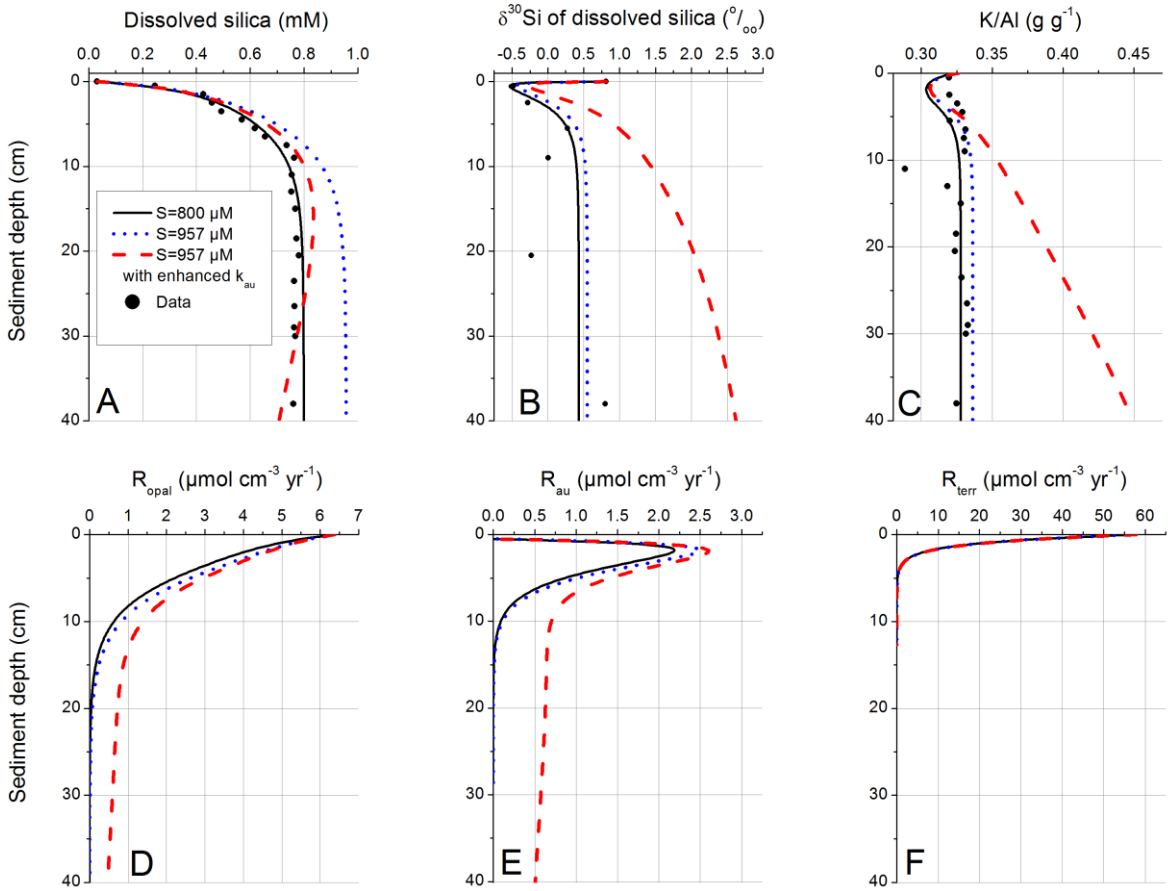

Fig. S7. Sensitivity of the model with respect to the solubility of biogenic opal (S). A. Dissolved silica concentration for the standard case (S = 800 µM), for S = 957 µM and for a simulation with S = 957 µM and enhanced precipitation (k_{au} standard equation + 0.2 µmol cm^{-3} yr^{-1}). B. Isotopic composition of dissolved silica. C. K/Al ratio in bulk sediment. D. Dissolution rate of biogenic opal. E. Precipitation rate of authigenic phases. F. Dissolution rate of terrigenous phases.

In the standard case, the kinetic constant for the precipitation of authigenic phases (k_{au} in µmol cm^{-3} yr^{-1}) was defined as (Tab. S4):

$$k_{au} = 5 \cdot e^{-0.5 \cdot x}$$

where x is sediment depth in cm. With this equation the precipitation rate was effectively suppressed below 15 cm sediment depth. In the sensitivity run, we added a constant term to allow for precipitation at depth:

$$k_{au} = 5 \cdot e^{-0.3 \cdot x} + 0.2$$

The silica removal induced by this additional term was large enough to reduce the dissolved silica concentrations to the observed level even though the dissolution rate of biogenic opal increased because the rapid precipitation caused a significant undersaturation of the pore fluids with respect to biogenic opal. However, the increase in the precipitation rate induced a massive increase in pore fluid $\delta^{30}Si$ and solid phase K/Al that is clearly not consistent with the data. Hence, it is very likely that the plateau value of dissolved silica attained below 10 cm sediment depth does not reflect a dynamic equilibrium between opal dissolution and authigenic phase precipitation as previously proposed (Van Cappellen and Qiu, 1997a) but rather the solubility of biogenic opal. The solubility of biogenic opal is reduced by the uptake of dissolved Al on opal surfaces that occurs when dissolved Al is released from sedimentary phases close to the sediment surface (Van Beusekom et al., 1997). It is likely that the low solubility of 800 µM is consequence of Al-uptake at the sediment surface (Dixit et al., 2001; Van Cappellen and Qiu, 1997a) where Al is provided by clay mineral dissolution.

References

Dixit, S., Cappellen, P. V., and Bennekom, A. J. V.: Processes controlling solubility of biogenic silica and pore water build-up of silicic acid in marine sediments, Marine Chemistry, 73, 333-352, 2001.

Ehlert, C., Doering, K., Wallmann, K., Scholz, F., Sommer, S., Grasse, P., Geilert, S., and Frank, M.: Stable silicon isotope signatures of marine pore waters - Biogenic opal dissolution versus authigenic clay mineral formation, Geochimica Et Cosmochimica Acta, 191, 102-117, 2016.

Frings, P. J., Clymans, W., Fontorbe, G., De La Rocha, C. L., and Conley, D. J.: The continental Si cycle and its impact on the ocean Si isotope budget, Chemical Geology, 425, 12-36, 2016.

Geilert, S., Hensen, C., Schmidt, M., Liebetrau, V., Scholz, F., Doll, M., Deng, L., Fiskal, A., Lever, M. A., Su, C.-C., Schlömer, S., Sarkar, S., Thiel, V. and Berndt, C.: On the formation of hydrothermal vents and cold seeps in the Guaymas Basin, Gulf of California, Biogeosciences, 15, 5715–5731 [online] Available from: https://doi.org/10.5194/bg-15-5715-2018, 2018.

Loucaides, S., Michalopoulos, P., Presti, M., Koning, E., Behrends, T., and Cappellen, P. V.: Seawater-mediated interactions between diatomaceous silica and terrigenous sediments: Results from long-term incubation experiments, Chemical Geology, 270, 68-79, 2010.

Michalopoulos, P. and Aller, R. C.: Early diagenesis of biogenic silcia in the Amazon delta: Alteration, authigenic clay formation, and storage, Geochimica et Cosmochimica Acta, 68, 1061-1085, 2004.

Taylor, S. R. and McLennan, S. M.: The geochemical evolution of the continental crust, Reviews of Geophysics, 33, 241-265, 1995.

Van Beusekom, j. E. E., Bennekom, A. J. V., Treguer, P., and Morvans, J.: Aluminium and silicic acid in water and sediments of the Enderby and Crozet Basins, Deep-Sea Research II, 44, 987-1003, 1997.

Van Cappellen, P. and Qiu, L.: Biogenic silica dissolution in sediments of the Southern Ocean. I. Solubility, Deep-Sea Research II, 44, 1109-1128, 1997a.

Van Cappellen, P. and Qiu, L.: Biogenic silica dissolution in sediments of the Southern Ocean. II. Kinetics, Deep-Sea Research II, 44, 1129-1149, 1997b.

Wallmann, K., Aloisi, G., Haeckel, M., Tishchenko, P., Pavlova, G., Greinert, J., Kutterolf, S., and Eisenhauer, A.: Silicate weathering in anoxic marine sediments, Geochimica et Cosmochimica Acta, 72, 2895-2918, 2008.

Wedepohl, K. H.: Environmantal influences on the chemical composition of shales and clay, Physics and Chemistry of the Earth, 8, 307-333, 1971.

Zheng, X., Beard, B. L., Reddy, T. R., Roden, E. E. and Johnson, C. M.: Abiologic silicon isotope fractionation between aqueous Si and Fe(III)-Si gel in simulated Archean seawater : Implications for Si isotope records in Precambrian sedimentary rocks, Geochemica Cosmochim. Acta, 187, 102–122, 2016.